Fabrication of a porous ZnRh2O4 photocathode for photoelectrochemical water splitting under visible light irradiation and a significant effect of surface modification by ZnO necking treatment

Sunao Kamimura,[1,2] Masanobu Higashi,[3] Ryu Abe,[3] and Teruhisa Ohno[1,2,4]*

[1]Department of Applied Chemistry, Faculty of Engineering, Kyushu Institute of Technology, 1-1 Sensuicho, Tobata, Kitakyushu 804-8550, Japan

[2] Research Center for Advanced Eco-fitting Technology, Kyushu Institute of Technology, 1-1 Sensuicho, Tobata, Kitakyushu 804-8550, Japan

[3] Graduate School of Engineering, Kyoto University, Katsura, Nishikyo-ku, Kyoto 615-8510, Japan

[4] ACT-C, Japan Science and Technology Agency, 4-1-8 Honcho, Kawaguchi-shi, Saitama 322-0012, Japan

KEYWORDS: photoelectrochemical water splitting, photocathode, photocatalyst

＊Corresponding author: tohno@che.kyutech.ac.jp

ABSTRACT

A porous $ZnRh_2O_4$ electrode was fabricated by an electrophoretic deposition method on a fluorine−doped tin oxide substrate, and photoelectrochemical water splitting under visible light irradiation (λ >420 nm) was performed. The porous $ZnRh_2O_4$ electrode exhibited a cathodic photocurrent under visible light irradiation and an extremely positive onset potential at +1.20 V vs. reversible hydrogen electrode (RHE) in aqueous Na_2SO_4 solution. ZnO necking treatment, by which effective contact between $ZnRh_2O_4$ particles is formed, afforded a significant increase in the photocurrent. The incident photon to current efficiencies (IPCEs) of the $ZnRh_2O_4$ and ZnO/$ZnRh_2O_4$ photocathodes were calculated to be ca. 8% and ca. 13% at 400 nm, respectively, at 0 V vs. RHE in aqueous Na_2SO_4 solution. H_2 evolution under visible light (λ >420 nm) was demonstrated using the $ZnRh_2O_4$ and ZnO/$ZnRh_2O_4$ photocathodes combined with a Pt electrode under an applied bias (0 V vs. RHE).

Introduction

Photoelectrochemical (PEC) water splitting utilizing semiconductor electrodes has attracted considerable attention as a potential means of converting solar energy into chemical energy in the form of usable hydrogen, which is a clean and renewable energy.[1-5] This research field was inspired by a report in 1972 by Fujishima and Honda, who demonstrated water splitting on a TiO_2 single crystal as a photoanode and a platinum counter electrode with an external bias under UV light irradiation.[6] Since almost 50% of the solar energy incident on the earth's surface falls within the visible−light energy range, recent research in this field has resulted in the development and fabrication of semiconductor electrodes capable of absorbing visible light. One goal of PEC water splitting is direct generation of H_2 over a *p*−type semiconductor electrode (photocathode) in combination with an *n*−type semiconductor electrode (photoanode) for O_2 generation from water without applying an external voltage under sunlight illumination. There have been many studies on high−efficiency visible light−responsive photoanodes such as WO_3,[7, 8] TaON,[9, 10] Fe_2O_3, [11-13] and $BiVO_4$,[14-17] but there have been few reports on photocathodes. Examples of the latter include Cu_2O,[18, 19] Rh-doped $SrTiO_3$,[20] and $CaFe_2O_4$ photocathodes,[21] which are *p*-type semiconductors with visible light responses.

The spinel oxide $ZnRh_2O_4$ with a band gap of ~2.1 eV is a unique material as a *p*−type metal oxide semiconductor.[22] The band gap of $ZnRh_2O_4$ originated from the ligand field splitting of octahedral−coordinated Rh^{3+} (Rh d^6 electronic configuration) between fully occupied t^6_{2g} and empty e^0_g orbitals, which correspond to valence band (VB) and conduction band (CB), respectively. Irie *et al.* reported photocatalytic H_2 evolution from water involving sacrificial reagents (formaldehyde HCHO) by using powdered $ZnRh_2O_4$ without any co−catalyst, and they experimentally suggested the band potential; the CB bottom and the VB top are located at ca. −1.1

V and ca. +0.1 V vs. SHE, respectively,[23] which is more negative than typical oxide semiconductors. Thus, $ZnRh_2O_4$ has sufficient potential as a photocathode for generation of H_2 from water. However, as far as we know, there has been no report on PEC water splitting by using a $ZnRh_2O_4$ electrode. The present research was carried out from this stand point.

We fabricated a porous $ZnRh_2O_4$ electrode by an electrophoretic deposition method on a fluorine−doped tin oxide (FTO) substrate, and demonstrated PEC water splitting under visible light irradiation. The porous $ZnRh_2O_4$ electrode exhibited cathodic photocurrent under visible light irradiation (λ >420 nm), and the photocurrent reached −100 $\mu A/cm^2$ at 0V vs. reversible hydrogen electrode (RHE) in aqueous Na_2SO_4 solution. Moreover, we introduced the ZnO necking treatment as a very suitable technique for improvement of photocurrent response of $ZnRh_2O_4$ electrode. The ZnO thin layer over $ZnRh_2O_4$ forms a space charge depletion region at the solid−solid interface (*p*−*n* heterojunction),[24,25] which results in better separation of the charge carriers. In addition, the ZnO thin film allows improved electrical contact between $ZnRh_2O_4$ particles. The incident photon to current efficiencies of $ZnRh_2O_4$ and ZnO/$ZnRh_2O_4$ photocathodes were calculated to be ca. 8% at 400 nm and ca. 13% at 400 nm, respectively, at 0 V vs RHE in aqueous Na_2SO_4 solution. In this report, the PEC property of the $ZnRh_2O_4$ photocathode is described, and the significant effect of ZnO necking treatment is discussed in conjunction with the structural and optical properties.

Experimental

Synthesis of $ZnRh_2O_4$ powder

$ZnRh_2O_4$ powder was synthesized by a solid state reaction method. ZnO (Wako, 99.0%) and Rh_2O_3 (Wako, >98.0%) as starting reagents were weighed stoichiometrically and mixed together

thoroughly. The mixture was calcined at 800 ℃ for 24 h in air. The obtained $ZnRh_2O_4$ powder was a brown color and the surface area was ca. 17 m^2g^{-1}.

Fabrication of a $ZnRh_2O_4$ electrode

The porous $ZnRh_2O_4$ electrode was fabricated by an electrophoretic deposition method on fluorine−doped tin oxide (FTO) substrate (Asahi Glass Co.). Electrophoretic deposition method was carried out in acetone (40 mL, Wako, 99.0%) containing $ZnRh_2O_4$ powder (50 mg) and iodine (30 mg, Wako, 99.8%), which was dispersed by sonication for 30 min. Two FTO electrodes (15 mm × 30 mm) were immersed parallel in the solution with a distance between them of 10 mm, and 6 V of bias was then applied between the electrodes for 3 min. After that, the electrodes were annealed at 400 ℃ for 1 h in air. The average amount of $ZnRh_2O_4$ deposited on FTO was 0.6 mg (area: 15 mm × 20 mm) by this electrophoretic deposition method. It should be noted that the electrophoretic deposition discribed above was optimized in the present study.

Necking treatment by ZnO precursor solution

The $ZnRh_2O_4$ electrode was coated with a ZnO thin film by sol–gel method,[26,27] using the following procedure. The zinc acetate $Zn(CH_3COO)_2 \cdot 2H_2O$ (Wako, 99.9%) was first dissolved in a 2−methoxyethanol (Wako, 99.0%) and monoethanolamine (Sigma−Aldrich, >99.0%) solution at room temperature. The molar ratio of monoethanolamine to zinc acetate was kept at 1.0 and the concentration of zinc acetate was 0.5 M. The mixed solution was stirred at room temperature for 24 h to obtain a clear and homogeneous ZnO precursor solution. The 50 μL of the ZnO precursor solution was dropped on the porous $ZnRh_2O_4$ electrode and then excess precursor solution was removed by spin−coating (1000 rpm, 30 sec). The electrode was dried in air at 200 ℃ for 5 min

on a hotplate. After this process had been repeated for a maximum of 7 times, the electrode was calcined in air at 400 ℃ for 1 h for crystallization of ZnO. Then the ZnO/$ZnRh_2O_4$ photocathode was obtained.

Characterization

The crystalline phases were characterized by using a powder X−ray diffraction (XRD) instrument (MiniFlex II, Rigaku Co.) with CuKα (λ=1.5418 Å) radiation (cathode voltage: 30 kV, current: 15 mA). The absorption properties of $ZnRh_2O_4$ (powder state) were measured using the diffuse reflection method with a UV/VIS/NIR spectrometer (V570, JASCO Co., Japan) attached to an integral sphere at room temperature. X−ray photoelectron spectroscopy (XPS) measurements were performed by using a Kratos AXIS Nova spectrometer (Shimazu Co.) with a monochromatic Al Kα X−ray source. The binding energy was calibrated by taking the carbon (C) 1s peak of contaminant carbon as a reference at 284.6 eV. Ultraviolet photoemission spectroscopy (UPS) was also carried out by using a Kratos AXIS Nova spectrometer. The UPS spectra were measured using He I excitation (21.2 eV) and recorded with a constant pass energy of 5 eV in the ultrahigh vacuum chamber of the XPS instrument. Applied bias was calibrated by determining the Fermi level of Au, which was deposited on the $ZnRh_2O_4$ electrode.

Photoelectrochemical (PEC) measurement

The PEC performance of the $ZnRh_2O_4$ and ZnO/$ZnRh_2O_4$ photocathodes was investigated in a three−electrode configuration using a silver−silver chloride (Ag/AgCl) reference electrode and a Pt coil counter electrode. The electrolyte was 0.1 M Na_2SO_4 solution (pH 6). The electrolyte was stirred and purged with Ar gas for 30 min before measurement. The measured potential vs.

Ag/AgCl was converted to RHE by Nernst's equation ($E_{RHE} = E_{Ag/AgCl} + 0.059\ pH + 0.197$). Linear sweep voltammetry and chronoamperometry measurements were carried out by using an automatic polarization system (HSV−110, Hokuto Denko Co.) under a Xe lamp equipped with an L−42 cut−off filter (SCF−50s−42L, SIGMAKOKI Co., Ltd.). The scan rate for the linear sweep voltammetry was 10 mV s^{-1}. The wavelength dependence of incident photon to current efficiency (IPCE) was measured by using a Xe lamp equipped with a band−pass filter centered at 400 nm, 450 nm, 500 nm, 550 nm, 600 nm, and 700 nm, respectively (All band−pass filters were purchased from Asahi Spectra Co., Ltd., and full width at half maximum was 10 nm.). The IPCE at each irradiation wavelength was calculated by the following equation:

$$\text{IPCE [\%]} = 1240 \times J\ [\text{mA/cm}^2] \times 100 / (\lambda\ [\text{nm}] \times I\ [\text{mW/cm}^2]),$$

where J is photocurrent density, λ is irradiation wavelength of the light−emitting diodes and I is irradiation intensity of incident light.

Analysis of products

PEC water splitting was performed in a gastight three−electrode configuration cell in which the $ZnRh_2O_4$ or $ZnO/ZnRh_2O_4$ photocathode, Pt wire and silver−silver chloride (Ag/AgCl) electrode were used as a working electrode, counter electrode and reference electrode, respectively. The electrolyte solution was 0.1 M Na_2SO_4, which was purged with Ar gas for ca. 40 min prior to the start of measurement. The cell was immersed in a cooling water bath to maintain solution temperature at 288 K during photoirradiation (Xe lamp, $\lambda > 420$ nm). Evolved H_2 gas was detected by an on−line gas chromatograph (GC) with a thermal conductivity detector (Agilent Technology Co. MicroGC) equipped with MS−5A column. It should be noted that the PEC water splitting was carried out by using flow reactor. Ar gas was used as the carrier gas.

Results and discussion

Structural, optical, and photoelectrochemical properties of the $ZnRh_2O_4$ electrode

Figure 1 shows the XRD pattern of the $ZnRh_2O_4$ electrode. All of the diffraction peaks coincide with those of the cubic phase of $ZnRh_2O_4$ (JCPDS 00−041−0134) and FTO substrate, with no other impurity phases being detectable. The calcination temperature of $ZnRh_2O_4$ was optimized in the present study (800℃−24h); at higher calcination temperatures (> 900℃), Rh_2O_3 was deoxidized into metal Rh, leading to a remarkable decrease of photocurrent of $ZnRh_2O_4$ electrode. At lower calcination temperature (< 700℃), unreacted Rh_2O_3 and ZnO remained.

Figure 2 shows a cross−sectional SEM photograph of the $ZnRh_2O_4$ electrode. A porous structure can be seen. The electrolyte solution will therefore penetrate into the pores of the $ZnRh_2O_4$ film. The $ZnRh_2O_4$ particles were ca. 200 nm in diameter with a thickness of ca. 2 μm. The $ZnRh_2O_4$ electrode prepared by the electrophoretic deposition method was easily peeled off by scratching with a nail and a spoon. Therefore, we annealed the $ZnRh_2O_4$ electrode at 400℃ for 1 h after the electrophoretic deposition method, resulting in a good adhesion property of the film due to the connection between $ZnRh_2O_4$ particles and the FTO substrate.

Figure 3 shows a UV−vis absorption spectrum of the $ZnRh_2O_4$ powder. The UV−vis spectrum has an absorption edge at around 600 nm, which corresponds to the optical band gap of $ZnRh_2O_4$. According to previous reports, $ZnRh_2O_4$ is an indirect energy gap material.[28,29] The optical absorption edge of $ZnRh_2O_4$ could be estimated from a Tauc plot ($(F(R\infty)h\nu)^n$ vs. $h\nu$, where n = 0.5 for an indirect bandgap (see **Fig. 3 inset**)), and the optical band gap of $ZnRh_2O_4$ was estimated to be ca. 2.0 eV, which is consistent with the early reports (~2.2 eV).[22,28]

To clarify the VB and CB band potentials, we measured the UPS spectrum of the $ZnRh_2O_4$ electrode in this study. Usually, band potential can be measured by electrochemical impedance spectroscopy, which can directly measure the capacitance of the Schottky junction. However, impedance measurements could not be completed for the porous $ZnRh_2O_4$ electrode because the electrolyte penetrated down to the FTO substrate. In this situation, UPS is a useful technique because the correlation between electrochemical potential and absolute potential of electrons has already been established.[30] **Figure 4** shows the UPS spectrum measured at 0 V and –9.2 V electrical bias. The cutoff of the UPS spectrum with the sample bias of 0 V could not be clearly observed, and a negative electrical bias was therefore applied. Applied bias was calibrated by determining the work function of Au, which was deposited on the $ZnRh_2O_4$. The features in the valence band and the entire spectrum remained unchanged with respect to the applied bias. The UPS spectrum started to rise near the Fermi energy, and a relatively sharp band that appeared at around 2 eV, which corresponds to the top of the valence band, was associated with *d* electron states, mostly likely the t_{2g} set of octahedral−coordinated Rh^{3+}. The work function of $ZnRh_2O_4$ was estimated to be 4.53 eV, which is good agreement with an early report.[22] Since the difference between work function and VB top is –0.50 V, the VB top and CB bottom potentials of $ZnRh_2O_4$ are considered to be located at ca. +0.6 V and –1.4 V vs. NHE (pH 0), respectively (see **Fig .5**).

Figure 6 shows current−potential curves of the $ZnRh_2O_4$ electrode in Ar−gas purged 0.1 M Na_2SO_4 solution (pH 6) under chopped visible light irradiation (Xe lamp, λ> 420 nm, 100 mW/cm^2). The $ZnRh_2O_4$ electrode exhibited a cathodic photocurrent in response to irradiation of visible light, indicating that $ZnRh_2O_4$ is a *p*−type oxide semiconductor. The cathodic photocurrent of $ZnRh_2O_4$ was increased with an increase in the applied potential, and its photocurrent density reached –110 μA/cm^2 at 0 V vs. RHE. As shown in the inset figure, onset potential of $ZnRh_2O_4$

was ca. +1.20 V vs. RHE, which compares favorably with any *p*−type semiconductor oxide such as Cu_2O (ca. +0.55 V vs. RHE),[18,19] $CaFe_2O_4$ (+1.24 V vs. RHE),[21] and $CuBi_2O_4$ (+1.05~1.1 V vs. RHE).[31]

Figure 7 shows the time courses of the cathodic photocurrent from the $ZnRh_2O_4$ electrode in 0.1 M Na_2SO_4 solution purged with Ar gas at 0 V vs. RHE under visible light irradiation (Xe lamp, λ> 420 nm, 100 mW/cm^2). When the electrode was exposed to incident light, a cathodic photocurrent rapidly flowed and then gradually decreased with time. After switching off the incident light, the current retuned to the initial state. Although there was a tendency for the photocurrent to decrease with time, observed amount of H_2 was agreed closely with the theoretical value based on Faraday's law, indicating that the cathodic photocurrent is due to the water reduction to produce, as will be discussed later (see **Fig. 14**). To clarify the stability of the $ZnRh_2O_4$ electrode, XPS measurement was done before and after the PEC reaction, as shown in **Fig. 8**. The peak positions of Zn *2p*, Rh *3d* and O *1s* were almost unchanged after the reaction. Moreover, we also analyzed the metal cation species in the electrolyte by ICP−AES after 1 h of PEC reaction. No detection of Zn and Rh ions indicated that those ions were not leached from $ZnRh_2O_4$ particles, implying that $ZnRh_2O_4$ is stable under PEC reaction.

Effect of ZnO necking treatment

As mentioned in the above section, we revealed that the porous $ZnRh_2O_4$ electrode acted as a photocathode and was applicable to PEC water splitting under visible light irradiation. However, in general, the photocurrent efficiency of a porous semiconductor electrode is limited due to the resistance loss at grain boundaries. This problem can be solved by necking treatment; that is, bridging semiconductor particles with binder materials for carrier conduction. Indeed, the water

oxidation photocurrent generated from a porous $LaTiO_2N$ electrode was improved by $TiCl_4$ necking treatment, where binder TiO_{2-x} layer leading to a decrease in resistance between $LaTiO_2N$ particles and/or the substrate.[32] Similar improvement of the photocurrent by necking treatment of TaON ($TaCl_5$ + NH_3 flow, or $TiCl_4$),[33-35] $SrNbO_2N$ ($NbCl_5$ + NH_3 flow),[36] and $BaTaO_2N$ ($TaCl_5$ + NH_3 flow)[37] electrodes has been reported.

We attempted to do necking treatment over the $ZnRh_2O_4$ electrode by using a zinc oxide (ZnO) precursor solution for further improvement of the photocurrent. Since *p*−*n* heterojunction diodes composed of *p*–type $ZnRh_2O_4$ and *n*–type ZnO have been reported,[24,25] the following two significant effects was anticipated by ZnO necking treatment: (1) bridging $ZnRh_2O_4$ particles with ZnO for smooth carrier conduction, and (2) a depletion layer formed at the $ZnRh_2O_4$/ZnO *p*–*n* junction could also assist in extracting photo–generated electrons from $ZnRh_2O_4$. We prepared the ZnO precursor solution by sol–gel method and then drop–casted it onto the $ZnRh_2O_4$ electrode with calcination. **Figure 9** shows the photocurrent response of the ZnO/$ZnRh_2O_4$ photocathode when the ZnO precursor solution was drop–casted 1 time. The ZnO/ $ZnRh_2O_4$ photocathode exhibited a photocurrent density of –250 $\mu A/cm^2$ at 0 V vs. RHE under visible light irradiation (λ >420 nm), which was ca. two-fold higher than that obtained on a bare electrode. The sharp rise beyond the onset potential and the tendency for photocurrent saturation in the high−potential region indicated that efficient charge carrier transfer has occurred by ZnO necking treatment. Taking into consideration that the onset potential was barely changed after ZnO necking treatment, it was highly possible that enhancement of photocurrent was due to an improvement of electrical contact between $ZnRh_2O_4$ particles by ZnO necking treatment rather than a formation of depletion layer at the $ZnRh_2O_4$/ZnO *p*–*n* junction, as will be discussed later.

To clarify the irradiation wavelength dependence of the photocurrent in bare and $ZnO/ZnRh_2O_4$ photocathodes, the action spectrum was acquired by determining the IPCEs at 0 V vs. RHE as a function of the irradiation wavelength (see **Fig. 10**). For the bare electrode, the IPCE action spectrum was blue−shifted by ∼100 nm relative to the optical absorption edge, and each IPCE was ca. 1%, 4%, and 8% with irradiation wavelengths at 500 nm, 450 nm, and 400 nm, respectively. Such a discrepancy between IPCE action spectrum and absorption spectrum has been observed in $CuNbO_3$ photocathode (blue−shifted by ca.∼150 nm), and the reason was suggested to be that band−edge electrons much less efficiently migrate to and transfer across the electrode interfaces.[38] According to the results of first−principles calculations of $ZnRh_2O_4$, the energy bands for VB maximum and CB minimum have a flat non−dispersed character, which contribute to the large density of states around the Fermi level and account for the large carrier effective mass and the small polaron mobility.[28] Therefore, the discrepancy between the IPCE action spectrum and absorption spectrum is considered to be caused mainly by recombination of photo−generated carriers near the absorption edge, as in the case of $CuNbO_3$ photocathode. For the $ZnO/ZnRh_2O_4$ photocathode, the IPCE action spectrum was in agreement with the optical absorption spectrum, and each of the IPCEs was increased to ca. two−fold higher than that of the bare electrode. These results suggested that the observed photocurrent in $ZnO/ZnRh_2O_4$ photocathode was due to light absorption by $ZnRh_2O_4$ rather than ZnO (bandgap ~ ca. 3.4 eV), and the ZnO necking treatment could assist the flow of electrons from $ZnRh_2O_4$ toward electrode−electrolyte interface, resulting in an improvement of IPCE.

To clarify the effect of necking treatment, we further investigated the physicochemical properties of the $ZnRh_2O_4$ electrode after the ZnO necking treatment. **Figure 11** shows the dependence of XRD patterns on the number of drop−casts (0, 1, 3, 5, and 7 times) of the ZnO

precursor solution. The ZnO diffraction peak intensities increased with an increase in the number of drop−casts, indicating that a crystalline ZnO phase could be formed on the $ZnRh_2O_4$ electrode by necking treatment. No ZnO diffraction peak were observed when the ZnO precursor solution was drop–casted 1 time, suggesting that ZnO on the $ZnRh_2O_4$ electrode were too small to be detected by XRD analysis. To further confirm the ZnO phase, we have investigated the XPS spectra of ZnO/$ZnRh_2O_4$ photocathodes (Fig. S1 in ESI). The XPS intensities of Zn $2p_{3/2}$ and $2p_{1/2}$, which peaked at 1022.4 eV and 1045.5 eV, respectively, were increased with an increase in the number of drop−casts, suggesting that the ZnO could be formed on $ZnRh_2O_4$ surface even when ZnO precursor solution was drop–casted 1 time.

Figure 12 shows top−view SEM images of the $ZnRh_2O_4$ electrodes before and after drop−casting of the ZnO precursor solution. Although there were many spaces among $ZnRh_2O_4$ particles in the untreated electrode (see Fig. 11c), the spaces were gradually filled with an increase in the number of drop−casts of the ZnO precursor solution (see Fig. 11d~e). The morphology of the $ZnRh_2O_4$ electrode was almost unchanged after drop−casting 1 time (see Fig. 11d). This suggested that most of the ZnO particles produced thin layers on the surfaces of $ZnRh_2O_4$ particles, which formed bridges between the $ZnRh_2O_4$ particles.

The cathodic photocurrent from the ZnO/$ZnRh_2O_4$ photocathode was strongly dependent on the number of drop−casts of the ZnO precursor solution. **Figure 13** shows the dependence of the photocurrent from the $ZnRh_2O_4$ electrode on the number of drop−casts (1, 3, 5, and 7). Increasing the number of drop−casts up to 7 times decreased the cathodic photocurrent and tended to cause a negative shift in the onset potential of the photocurrent. Basak *et al.* have been studied the effect of thickness on electrical property of ZnO thin films, which prepared by sol−gel method;[39] as thickness of the ZnO thin film was increased, the ZnO film became more porous and hence the

amount of adsorbed oxygen at the grain boundary was increased, resulting in more carriers being trapped and an increase in resistivity increased. Therefore, we consider that an effect of ZnO necking treatment is mainly to bridging $ZnRh_2O_4$ particles for carrier conduction, similar to dye-sensitized solar cells.[40] Moreover, ZnO thin film coating is an important role for enhancement of photocurrent of $ZnRh_2O_4$ electrode because of smooth carrier conduction.

Finally, the Faradaic efficiencies of bare and ZnO/$ZnRh_2O_4$ photocathodes were evaluated by analysis of evolved H_2 gases. **Figure 14** shows the time courses of H_2 evolution over bare and ZnO/$ZnRh_2O_4$ photocathodes under visible light irradiation (λ >420 nm) at 0 V vs. RHE. For both sample, the amount of H_2 evolved was slightly less than half of the electrons passing through the outer circuit ($e^-/2$, shown as a dotted line), possibly due to backward reaction on the Pt counter electrode and/or an induction period. The Faradaic efficiencies of bare and ZnO/$ZnRh_2O_4$ photocathodes were estimated to be ca. 77% and ca. 85%, respectively. These results show that bare and ZnO/$ZnRh_2O_4$ photocathodes can actually work for water splitting in PEC cell, and ZnO necking treatment promotes H_2 evolution under visible light irradiation. The durability of ZnO/$ZnRh_2O_4$ photocathode was tested for 1.5 h (the current was measured simultaneously with the gas evolution as in the inset). The initial photocurrent of ZnO/$ZnRh_2O_4$ (ca.−0.4 mA) decreased with time and reached about ca.−0.05 mA after 1.5 h. This does not represent a good durability of ZnO/$ZnRh_2O_4$ and appears to be a characteristic of ZnO because bare $ZnRh_2O_4$ electrode was stable upon PEC reaction (Fig. S2 in ESI). Indeed, we analyzed the metal cation species in the electrolyte by ICP−AES after 1.5 h of PEC reaction. Although no Rh ions were detected in the electrolyte, the Zn ions were detected. Moreover, XPS analysis of ZnO/$ZnRh_2O_4$ photocathode revealed that the peak intensities of Zn $2p_{3/2}$ and $2p_{1/2}$ were decreased after 1.5 h of PEC reaction (Fig. S3 in ESI), suggesting that ZnO was dissolved into electrolyte upon PEC

reaction, resulting in a decrease of photocurrent with time. Thus, the ZnO necking treatment improves the PEC performance of the $ZnRh_2O_4$ electrode, while there are still issues about stability. Further research is required to improve the PEC performance avoiding degradation processes of $ZnO/ZnRh_2O_4$ photocathode by loading the hydrogen−evolving catalyst such as Pt, MoS_{2+x} and RuO_2.

Conclusions

A porous $ZnRh_2O_4$ electrode was fabricated by an electrophoretic deposition method on a fluorine−doped tin oxide substrate, and it showed photoelectrochemical water splitting under visible light irradiation (λ >420 nm) for the first time. The porous $ZnRh_2O_4$ electrode exhibited a cathodic photocurrent under visible light irradiation and its photocurrent density reached –110 $\mu A/cm^2$ at 0 V vs. RHE in aqueous Na_2SO_4 solution. Furthermore, we introduced the ZnO necking treatment as a very suitable technique for improvement of photocurrent response of $ZnRh_2O_4$ electrode; the photocurrent of $ZnO/ZnRh_2O_4$ photocathode was enhanced to ca. two−fold higher than that of the bare electrode. The incident photon to charge carrier efficiencies (IPCEs) of the $ZnRh_2O_4$ and $ZnO/ZnRh_2O_4$ photocathodes were calculated to be ca. 8% and ca. 13% at 400 nm, respectively, at 0 V vs. RHE in aqueous Na_2SO_4 solution. The hydrogen evolution from $ZnRh_2O_4$ and $ZnO/ZnRh_2O_4$ photocathodes was confirmed with the faradaic efficiency of ca. 77% and ca. 85%, respectively.

Acknowledgements

The authors thank Prof. Shintaro Ida of Kyushu University for valuable contributions to this study. The authors also thank Prof. Tetsuya Haruyama, Prof. Naoya Murakami, Dr. Keisuke

Hamada, and Mr. Kai Tanaka of Kyushu Institute of Technology for their valuable contributions to this study. This work has been supported by a grant from Advanced Catalytic Transformation program for Carbon utilization (ACT−C), Japan Science and Technology Agency (JST).

Notes and references

1 A. Kudo and Y. Miseki, *Chem. Soc. Rev*., 2009, **38**, 253−278.

2 R. Abe, *J. Photochem. Photobiol. C*, 2010, **11**, 179−209.

3 D. G. Nocera, *Acc. Chem. Res*., 2012, **45**, 767−776.

4 K. Sivula, *J. Phys. Chem. Lett*., 2013, **4**, 1624−1633.

5 T. Hisatomi, J. Kubota and K. Domen, *Chem. Soc. Rev.*, 2014, **43**, 7520−7535.

6 A. Fujishima and K. Honda, *Nature*, 1972, **238**, 37−38.

7 K. Sivula, F. L. Formal and M. Grätzel, *Chem. Mater.*, 2009, **21**, 2862−2867.

8 J. A. Seabold and K. S. Choi, *Chem. Mater.*, 2011, **23**, 1105–1112.

9 M. Higashi, K. Domen and R. Abe, *Energy Environ. Sci.*, 2011, **4**, 4138−4147.

10 M. Higashi, K. Domen and R. Abe, *J. Am. Chem. Soc*., 2012, **134**, 6968−6971.

11 A. Kay, I. Cesar and M. Grätzel, *J. Am. Chem. Soc*., 2006, **128**, 15714−15721.

12 Y. S. Hu, A. Kleiman-Shwarsctein, A. J. Forman, D. Hazen, J. N. Park and E. W. McFarland, *Chem. Mater.*, 2008, **20**, 3803−3805.

13 K. Sivula, R. Zboril, F. Le Formal, R. Robert, A. Weidenkaff, J. Tucek, J. Frydrych and M. Grätzel, *J. Am. Chem. Soc*., 2010, **132**, 7436−7444.

14 K. Sayama, A. Nomura, T. Arai, T. Sugita, R. Abe, M. Yanagida, T. Oi, Y. Iwasaki, Y. Abe and H. Sugihara, *J. Phys. Chem. B*, 2006, **110**, 11352−11360.

15 Y. H. Ng, A. Iwase, A. Kudo and R. Amal, *J. Phys. Chem. Lett.*, 2010, **1**, 2607−2612.

16 T. W. Kim and K. S. Choi, *Science*, 2014, **343**, 990−994.

17 B. J. Trześniewsk and W. A. Smith, *J. Mater. Chem. A*, 2016, **4**, 2919−2926.

18 S. D. Tilley, M. Schreier, J. Azevedo, M. Stefik and M. Grätzel, *Adv. Funct. Mater.*, 2014, **24**, 303−311.

19 A. Paracchino, V. Laporte, K. Sivula, M. Grätzel and E. Thimsen, *Nat. Mater*., 2011, **10**, 456−461.

20 K. Iwashina and A. Kudo, *J. Am. Chem. Soc.*, 2011, **133**, 13272−13275.

21 S. Ida, K. Yamada, T. Matsunaga, H. Hagiwara, Y. Matsumoto and T. Ishihara, *J. Am. Chem. Soc.*, 2010, **132**, 17343−17345.

22 H. Mizoguchi, M. Hirano, S. Fujitsu, T. Takeuchi, K. Ueda and H. Hosono, *Appl. Phys. Lett.*, 2002, **80**, 1207−1209.

23 Y. Takimoto, T. Kitta and H. Irie, *Int. J. Hydrogen Energy*, 2012, **37**, 134−138.

24 H. Ohta, H. Mizoguchi, M. Hirano, S. Narushima, T. Kamiya and H. Hosono, *Appl. Phys. Lett.*, 2003, **82**, 823−825.

25 T. Kamiya, S. Narushima, H. Mizoguchi, K. Shimizu, K. Ueda, H. Ohta, M. Hirano and H. Hosono, *Adv. Funct. Mater.*, 2005, **15**, 968−974.

26 M. Ohyama, H. Kozuka and T. Yoko, *Thin Solid Films*, 1997, **306**, 78−85.

27 B. S. Ong, C. S. Li, Y. Li, Y. Wu and R. Loutfy, *J. Am. Chem. Soc*., 2007, **129**, 2750−2751.

28 N. Mansourian-Hadavi, S. Wansom, N. H. Perry, A. R. Nagaraja and T. O. Mason, *Phys. Rev. B*, 2010, **81**, 075112-1−075112-6.

29 D. J. Singh, R. C. Rai, J. L. Musfeldt, S. Auluck, N. Singh, P. Khalifah, S. McClure and D. G. Mandrus, *Chem. Mater.* 2006, **18**, 2696−2700.

30 W. J. Chun, A. Ishikawa, H. Fujisawa, T. Takata, J. N. Kondo, M. Hara, M. Kawai, Y. Matsumoto and K. Domen, *J. Phys. Chem. B*, 2003, **107**, 1798−1803.

31 N. T. Hahn, V. C. Holmberg, B. A. Korgel and C. B. Mulllins, *J. Phys. Chem. C*, 2012, **116**, 6459−6466.

32 N. Nishimura, B. Raphael, K. Maeda, L. L. Gendre, R. Abe, J. Kubota and K. Domen, *Thin Solid Films*, 2010, **518**, 5855−5859.

33 R. Abe, T. Takata, H. Sugihara and K. Domen, *Chem. Lett*., 2005, **34**, 1162−1163.

34 R. Abe, M. Higashi and K. Domen, *J. Am. Chem. Soc*., 2010, **132**, 11828−11829.

35 S. S. Gujral, A. N. Simonov, M. Higashi, R. Abe and L. Spiccia, *ChemElectroChem*., 2015, 2, 1270−1278.

36 K. Maeda, M. Higashi, B. Siritanaratkul, R. Abe and K. Domen, *J. Am. Chem. Soc*., 2011, **133**, 12334−12337.

37 M. Higashi, K. Domen and R. Abe, *J. Am. Chem. Soc*., 2013, **135**, 10238−10241.

38 U. A. Joshi, A. Palasyuk and P. A. Maggard, *J. Phys. Chem. C*, 2011, **115**, 13534−13539.

39 S. Mridha and D. Basak, *Mater. Res. Bulletin*, 2007, **42**, 875−882.

40 Q. B. Meng, K. Takahashi, X. T. Zhang, I. Sutanto, T. N. Rao, O. Sato and A. Fujishima, *Langmuir*, 2003, **19**, 3572−3574.

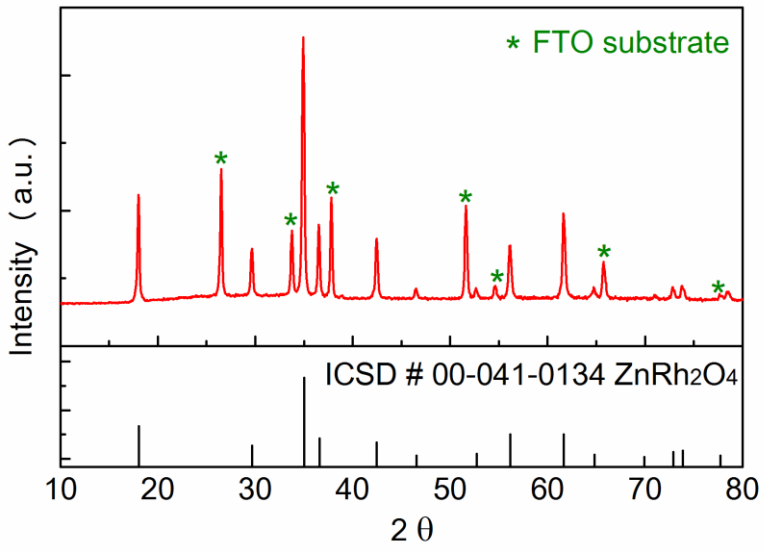

Figure 1. XRD pattern of $ZnRh_2O_4$ electrode.

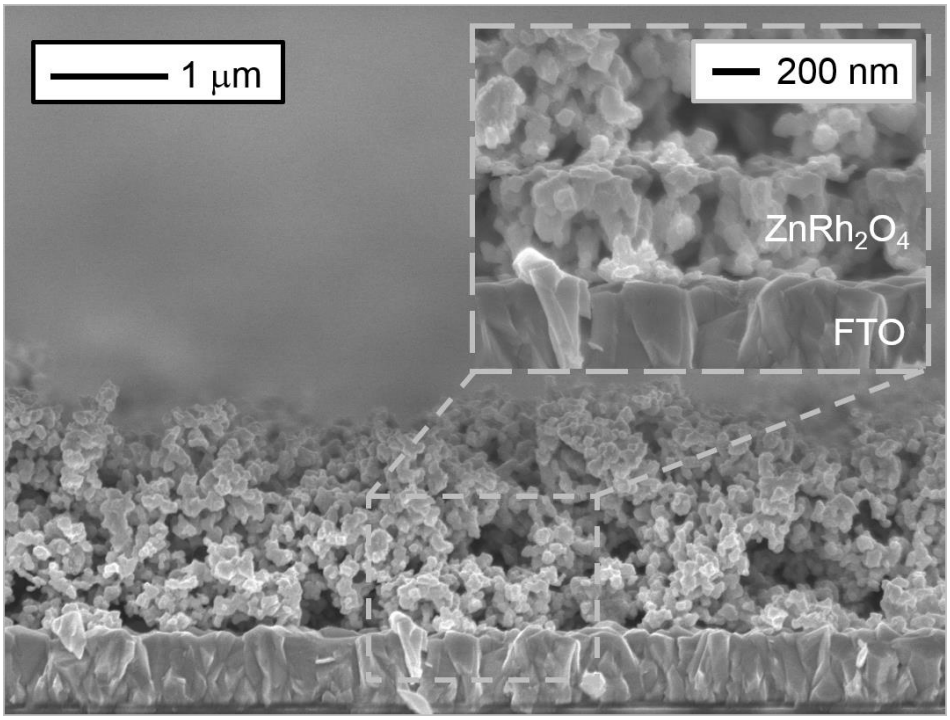

Figure 2. Cross−sectional SEM image of $ZnRh_2O_4$ electrode.

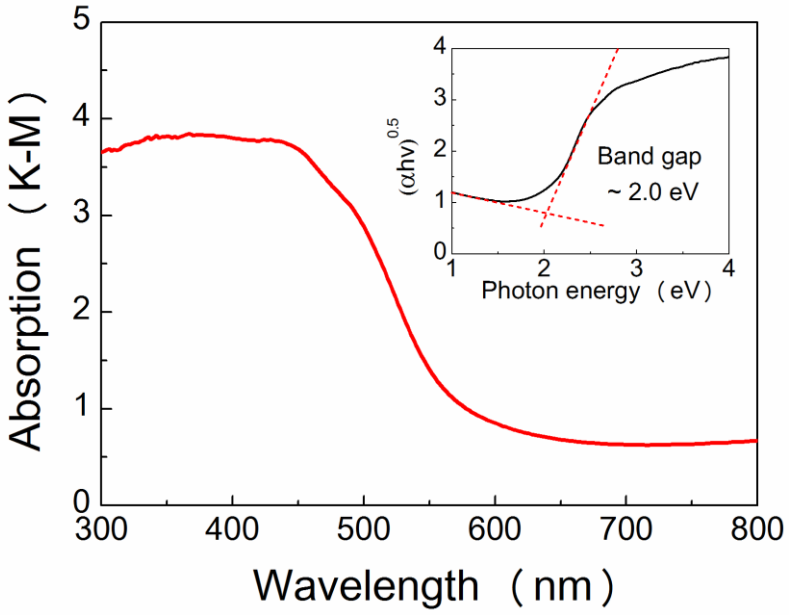

Figure 3. UV−vis spectrum of $ZnRh_2O_4$ powder. Optical band gap was determined by Tauc plots, as shown in the insets.

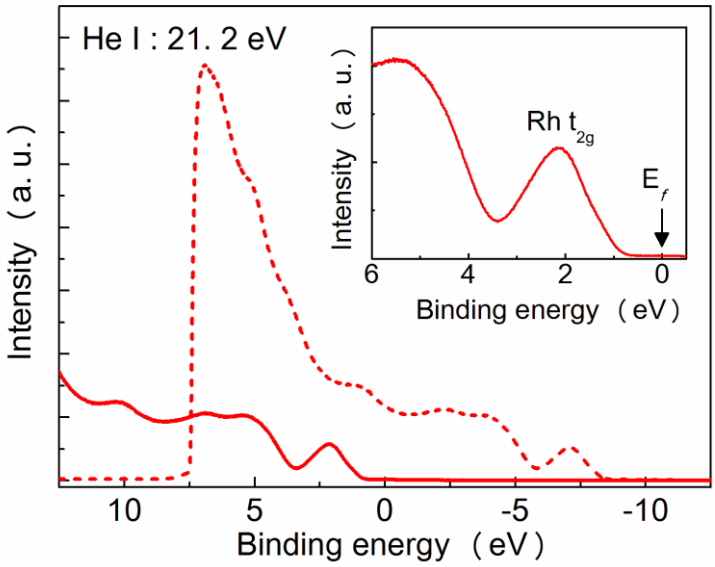

Figure 4. UPS spectra of $ZnRh_2O_4$ electrode measured at non−bias (solid line) and −9.2 V (dotted line).

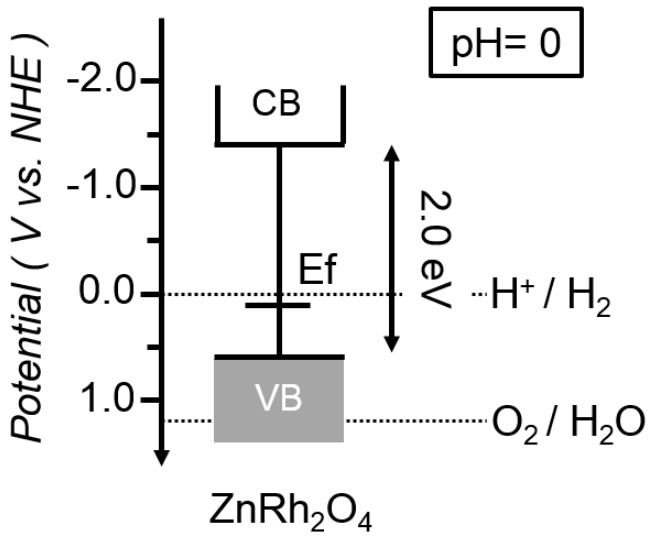

Figure 5. Band position of $ZnRh_2O_4$ determined by UPS measurements.

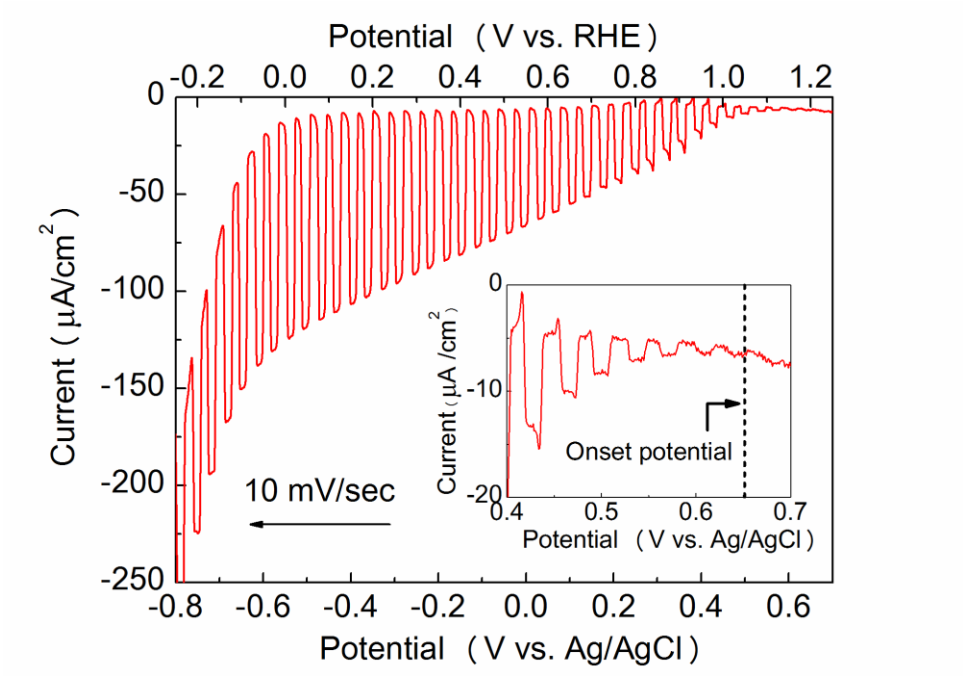

Figure 6. Current−potential curves in aqueous 0.1 M Na_2SO_4 solution (pH 6) under chopped visible light irradiation (λ> 420 nm, 100 mW/cm^2) for $ZnRh_2O_4$ electrode.

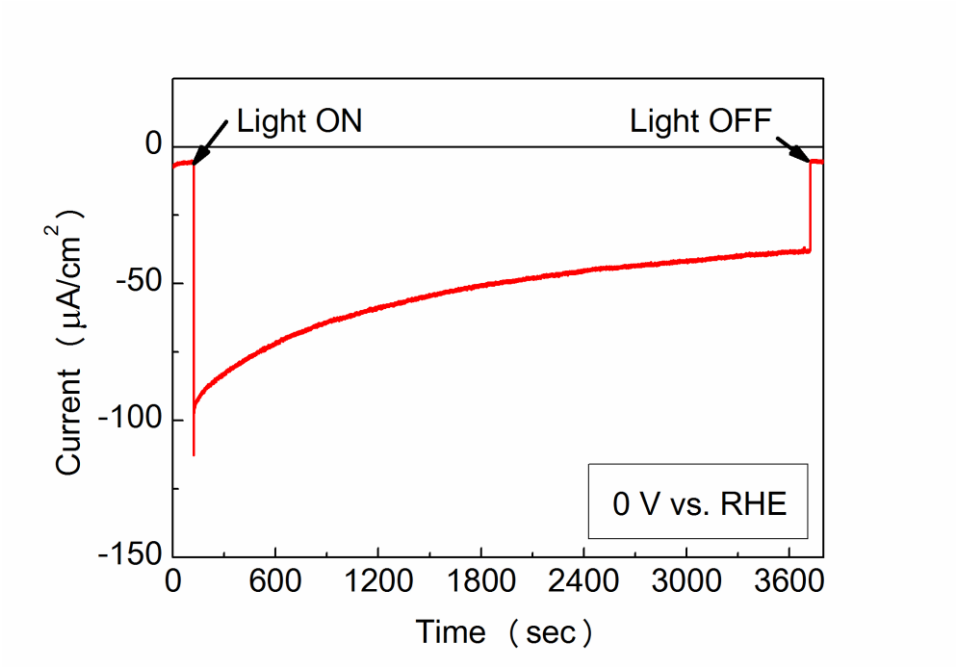

Figure 7. Time course for the photocurrent of $ZnRh_2O_4$ electrode in aqueous 0.1 M Na_2SO_4 solution (pH 6) at 0 V vs. RHE under visible light irradiation (Xe lamp, λ> 420 nm, 100 mW/cm^2).

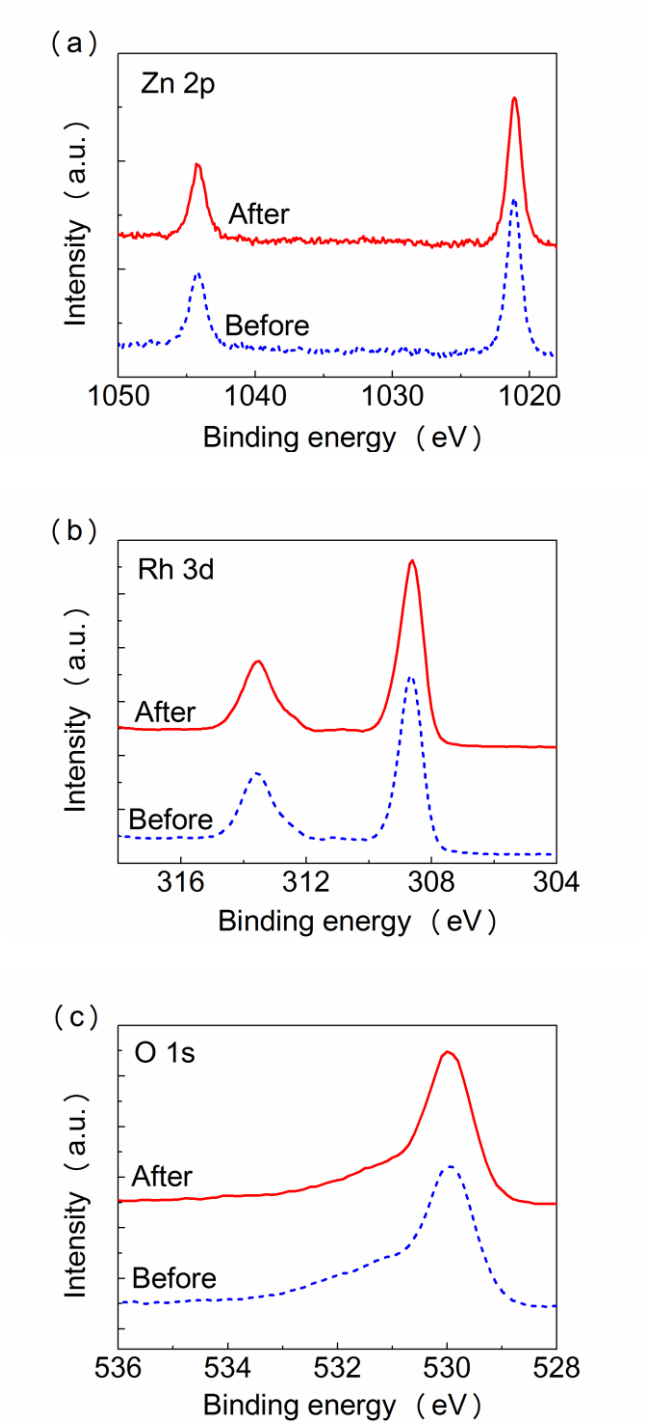

Figure 8. XPS spectra of $ZnRh_2O_4$ electrode before and after 1 h of photoirradiation (λ> 420 nm, 100 mW/cm^2) in aqueous 0.1 M Na_2SO_4 solution (pH 6) at 0 V vs. RHE.

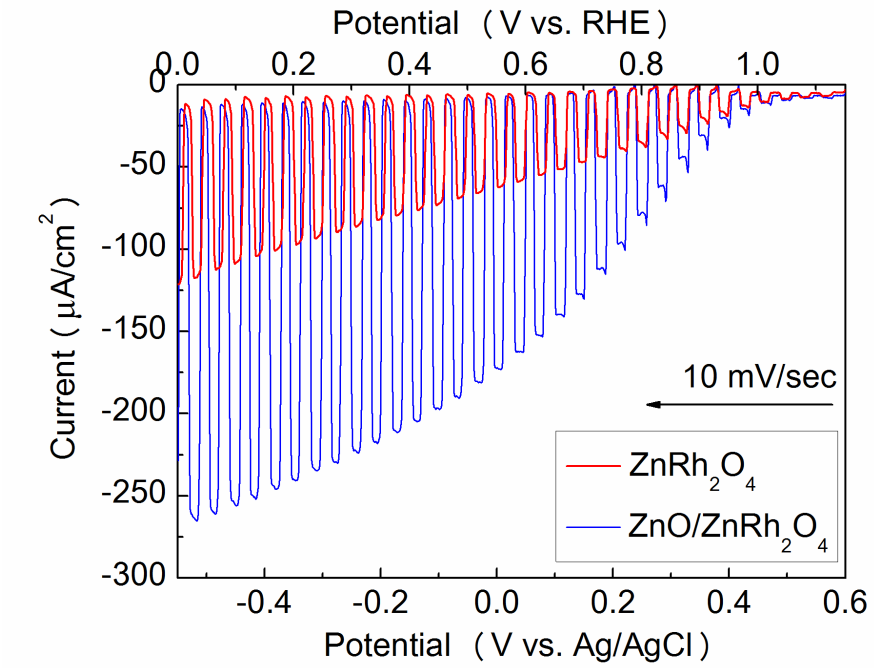

Figure 9. Current−potential curves in aqueous 0.1 M Na_2SO_4 solution (pH 6) under chopped visible light irradiation (λ> 420 nm, 100 mW/cm^2) for $ZnRh_2O_4$ electrode and $ZnO/ZnRh_2O_4$ electrode (ZnO precursor solution was drop–casted 1 time).

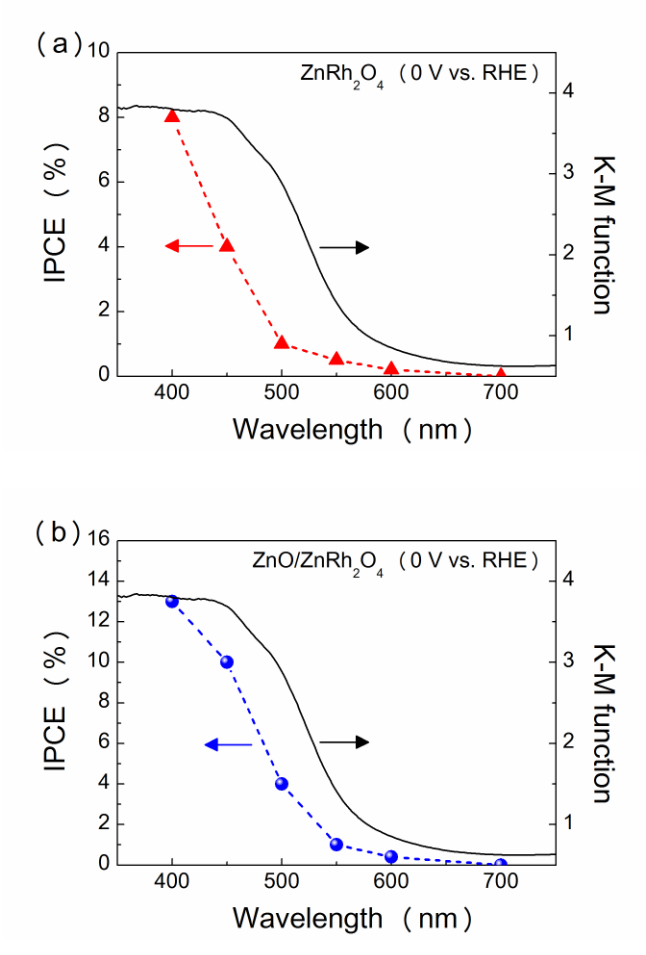

Figure 10. IPCE dependence on the wavelength of (a) $ZnRh_2O_4$ and (b) ZnO/ $ZnRh_2O_4$ photocathode at 0 V vs. RHE in aqueous 0.1 M Na_2SO_4 solution.

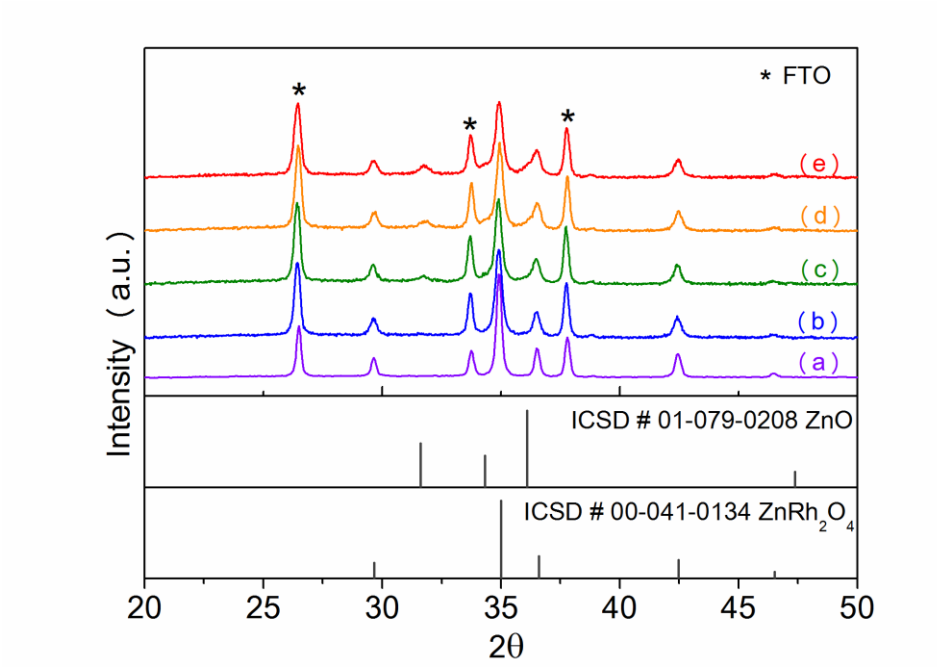

Figure 11. XRD pattern of (a) bare $ZnRh_2O_4$ electrode, (b) ZnO precursor solution was drop–casted 1 time, (c) 3 times, (d) 5 times, and (e) 7 times.

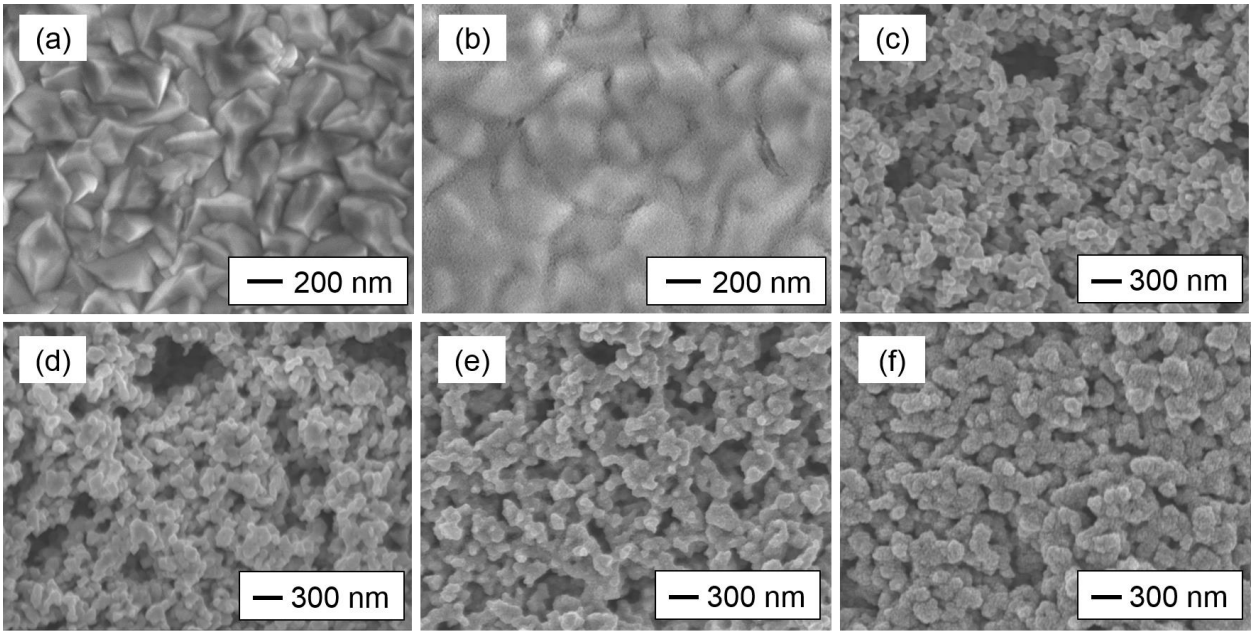

Figure 12. SEM image of (a) FTO substrate, (b) 1 times ZnO drop−casted FTO substrate, (c) bare $ZnRh_2O_4$ electrode, (d) ZnO precursor solution was drop–casted 1 time (e) 3 times, and (f) 7 times.

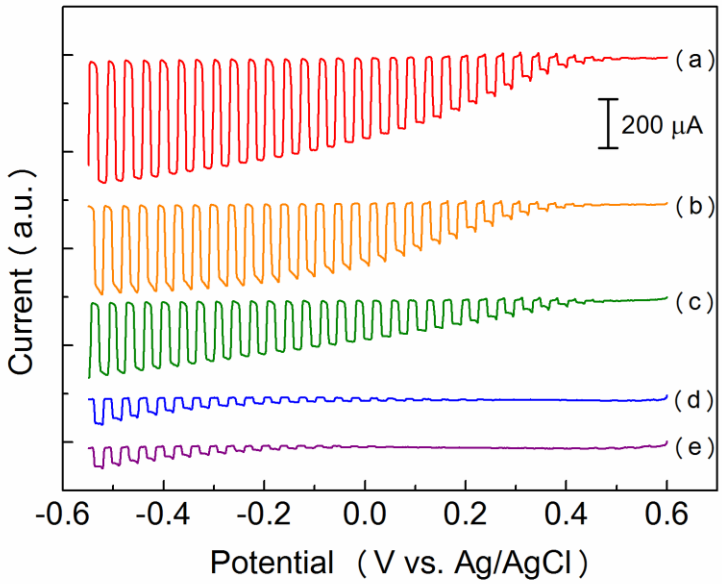

Figure 13. Current−potential curves in aqueous 0.1 M Na_2SO_4 solution (pH 6) under chopped visible light irradiation (λ> 420 nm) of $ZnRh_2O_4$ electrode when ZnO precursor solution was drop–casted (a) 1 time, (b) 2 times, (c) 3 times, (d) 5 times and (e) 7 times. Electrode aera was ca. 2 cm^2.

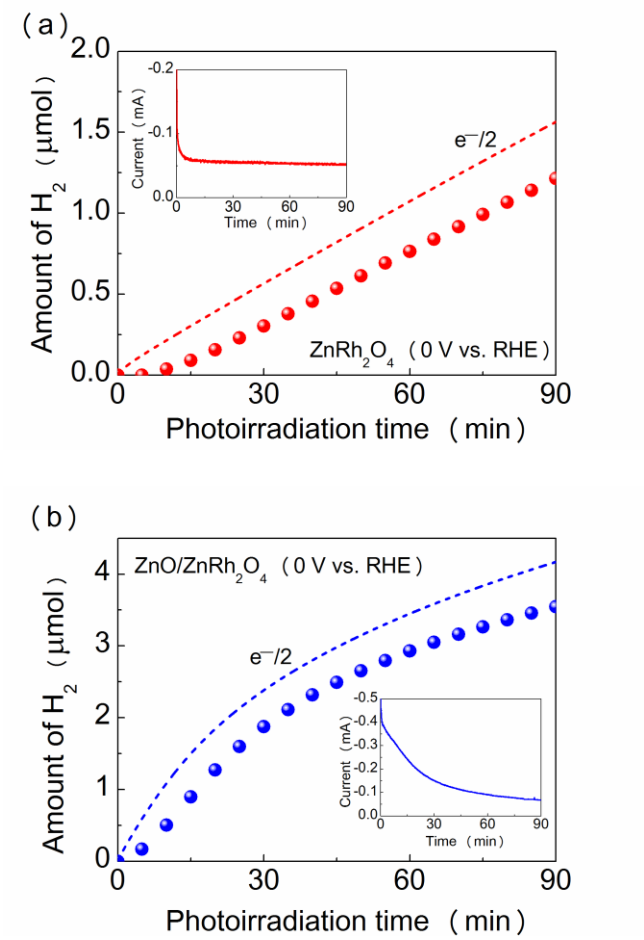

Figure 14. Time courses of gas evolution for (a) $ZnRh_2O_4$ electrode and (b) $ZnO/ZnRh_2O_4$ electrode, combined with Pt-wire counter electrode and Ag/AgCl reference electrode, in aqueous 0.1 M Na_2SO_4 solution (pH 6) with applied bias 0 V vs. RHE under visible light irradiation ($\lambda >$ 420 nm). The insets indicate the time courses of the cathodic photocurrent, where electrode aera was ca. 3 cm^2.